A Non-Equilibrium Nucleation Model to Calculate the Density of State and Its Application to the Heat Capacity of Stoichiometric UO$_2$

Ivaldo Leão Ferreira[1] ⓘ

Abstract

In this paper, the molar specific heat capacity is theoretically predicted for stoichiometric UO$_{2.00}$ in the temperature range from 0 K to 3000 K. The λ-phase transition at 2670 ± 30 K and its transformation heat is predicted. Furthermore, the occurrence of a small discontinuity corresponds to the rapid and simultaneous magnetic, electrical, and structural transition to occurs at 30.5 K and unit cell change at 30.8 K have been reported. Debye temperature assumed for UO$_{2.00}$ is $\Theta_D \cong 900 K$. The Gibbs–Thomson coefficient applied to calculate the density of state is derived from considering the strain in the interior of the crystal due to the free surface of the solid grain. A new relation between surface tension and surface energy during solid–liquid nucleation is established, allowing calculating Gibbs–Thomson in terms of surface tension or surface energy. Theoretical predictions are plotted against experimental scatter.

Keywords Density of state · Molar heat capacity of oxides · Molar specific heat of stoichiometric UO$_{2.00}$ · Non-equilibrium nucleation

1 Introduction

The specific heat capacity of uranium dioxide is influenced by several physical phenomena such as *λ-phase* transition, stoichiometry, Frenkel oxygen lattice disorder, Schottky defects, *λ-phase* transition. An extensive review and thermophysical properties can be found in [1, 2]. Huntzicker and Westrum determined experimentally the molar specific heat from the temperature range from 5 K to 350 K [3], Grønvold *et al.* from 304 to 1006 [4], while Ronchi *et al.* measuring in the interval 1700–2900 K by applying laser flash technique with two shots of 1 ms and 10 ms through an

✉ Ivaldo Leão Ferreira
  ileao@ufpa.br

1   Faculty of Mechanical Engineering, Federal University of Pará, UFPA, Augusto Corrêa Avenue
    1, Belém, PA 66075-110, Brazil

analytical solution confirmed by a good agreement between both datasets [5]. The authors compared their experimental data up to 2600 K, close to the interpolating curve by Fink and Petri [6]. According to Ronchi *et al.*, the increase of molar heat capacity of stoichiometric UO_2 could be interpreted as mainly due to Frenkel pair formation, which for the temperature range between 2600 K and 2700 K, promotes order–disorder λ-transition in the anion sublattice. Above this range, the experimental measurements are less precise [5]. Above 2700 K to the melting point Fink and Petri [6] handled as a constant heat capacity of 620 $J.kg^{-1}K^{-1}$. Ronchi *et al.* considered increasing and linearly dependent on temperature. Another important λ-type transition occurs at 28.7 K observed by Jones *et al.* [3, 7], assumed from high-temperature paramagnetic to low-temperature anti-ferromagnetic state transition. Lately, reported as two distinct phenomena: a simultaneous magnetic, electrical, and structural transition to occurs at 30.5 K (Mott Transition) and unit cell change at 30.8 K [8]. Other properties of uranium dioxide have been observed such as piezomagnetism and magneto-elastic memory effect [9] and anisotropy of thermal conductivity [10]. Ferreira *et al.* proposed a model for predicting molar specific heat capacity of phases and compounds by calculating the density of state based on the number of modes of the critical nucleus [11]. Lately, it was applied for pure elements and compounds [12] and transition metals [13].

In the present paper, the previously proposed model [11] is applied to stoichiometric uranium dioxide. Analytical predictions are plotted against experimental scatter.

2 Numerical Approach and Analytical Models

One of the major steps in calculating molar specific heat is the determination of the Density of State. Ferreira *et al.* [11] metals, phases, and compounds, Ferreira *et al.* [12] pure metals and compounds and transition metals Ferreira [13] found the nucleation step plays the most important role in the determination of the Density of State as it establishes the number of modes for a certain degree of undercooling. The original derivation of nucleation formulation was based on the same assumptions applied to the liquid–gas transformation. But in the solid–liquid transformation, once the critical nucleus is formed, surface stress gives rise to strain in the interior of the crystal as formulated by Gurtin and Murdoch [14]. As the critical nucleus radius decreases by a deviation from the equilibrium conditions, the internal strain is magnified. The region affected by this internal strain increases since this length scale depends only on the physical properties and geometry. Kim and Lee [15], while analyzing the dependency of the melting point of nanoparticles and wires, the size dependency of the surface, proposed a semi-empirical thermodynamic model. The authors extended the model for a wide range of elements such as FCC (Au, Pt, Ni), HCP (Mg), and BCC (W). They found good agreement with experimental data. Wu *et al.* [16] proposed a correction of the surface energy in the Gibbs–Thomson equation previously proposed by Kim and Lee. The surface energy should not vary with radius unless internal stress due to the free surface plays an important role. As radius decreases, stress

in the surface increases, following the observation of Gurtin and Murdoch [14]. Hence, the authors considered the surface stress tensor for the stress localized in the surface region and assumed physical properties in the neighborhood of the grain surface are different from those in the interior. The authors demonstrated the magnitude of the surface stress for a solid sphere of radius r is a uniform pressure given by,

$$s = \frac{2\sigma}{r(1 + \alpha)} \tag{1}$$

and,

$$\alpha = \frac{2[\sigma + 2(\lambda_0 + \mu_0)]}{r(3\lambda + 2\mu)} \tag{2}$$

where s is the isotropic surface stress, the σ is the surface tension, λ, λ_0, μ and μ_0 are the Lamé moduli.

The reason why the semi-empirical equation proposed by Kim and Lee [15] reasonably predicts the deviation of nucleation temperature by correcting the surface energy could only be explained by the strain in the interior of the Crystal, which increases as the nucleation radius decreases. The correction proposed for surface-energy by the authors is written quantitatively in terms of the first nearest neighbors' atoms interatomic distance for crystalline materials under non-equilibrium r, and the equilibrium r_{Eq} conditions. Wu *et al.* [16] corrected Kim and Lee's final spherical nucleus radius, providing a better agreement with the experimental data. Nevertheless, as the equilibrium radius $r_{Eq} = r + \delta \equiv constant$, must remain constant for any given radius r. If the radius r decreases by a certain amount, δ must increase by the same amount. Consequently, a new equation for correcting the surface energy as a function of $\delta = f(r)$ must be proposed.

Figure 1 presents the schematic representation of nucleation under equilibrium and non-equilibrium conditions and the relation between the r_{Eq}, $\delta(r)$ and r. Firstly, the new equation will be derived on the same basis as Kim and Lee [15] and Wu *et al.* [16], except for the equilibrium radius $r = r_{eq}$ that remains constant, and r is defined as $r = r_{eq} - \delta(r)$, due to non-equilibrium nucleation. Secondly, a new derivation based on the surface stress tension and superficial energy will be shown.

2.1 First Derivation

The relation between the equilibrium surface and non-equilibrium surfaces provides,

$$\frac{A_{equilibrium\,surface}}{A_{non-equilibrium\,surface}} = \frac{r_{eq}^2}{(r_{eq} - \delta)^2} = \frac{1}{\left(1 - \frac{\delta}{r_{eq}}\right)^2} \tag{3}$$

where $0 \leq \delta < (r_{eq} - r_{Max})$.
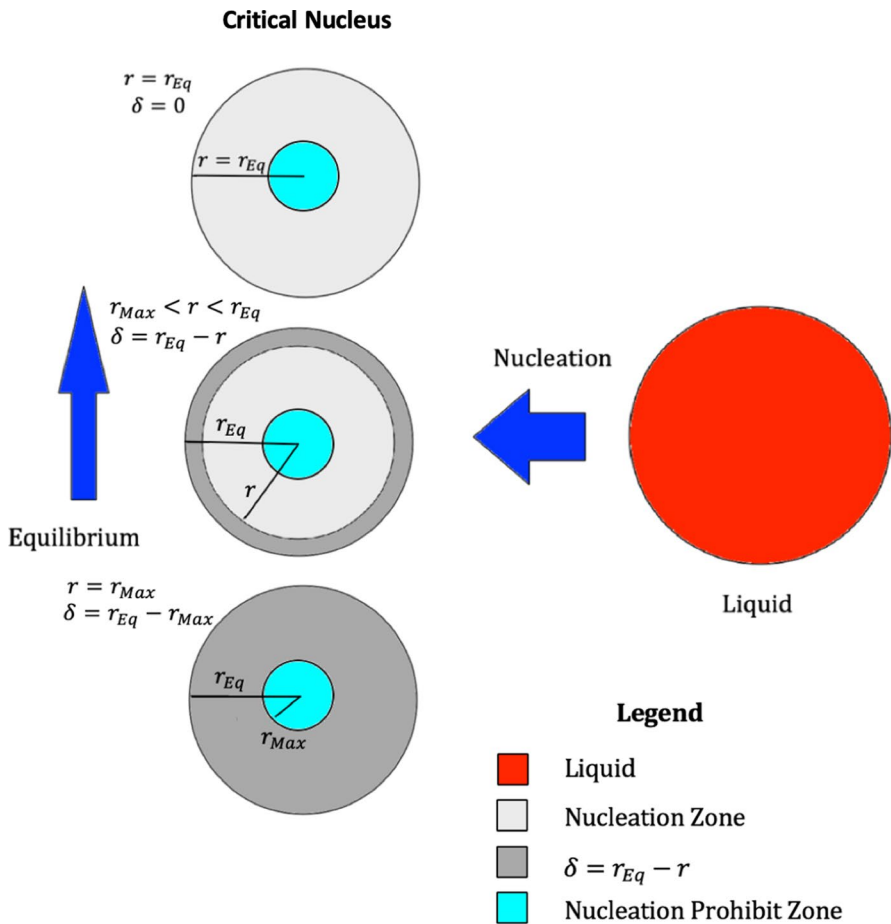
Critical Nucleus

Fig. 1 Schematic representation of nucleation of critical grain regarding equilibrium and non-equilibrium conditions

Now, rewriting Gibbs–Thomson with this view,

$$\Gamma = \frac{\gamma_{SL}^{0}}{\left(1 - \frac{\delta}{r_{eq}}\right)^{2} \Delta S_{\forall}} \tag{4}$$

and, the surface energy in terms of δ,

$$\gamma_{SL} = \frac{\gamma_{SL}^{0}}{\left(1 - \frac{\delta}{r_{eq}}\right)^{2}} \tag{5}$$

By calculating a mean value $\overline{\gamma_{SL}}$ for the surface energy,

$$\overline{\gamma_{SL}} = \frac{\gamma_{SL}^0}{\frac{\pi}{4}} \int_0^{\frac{\pi}{4}} \frac{\gamma_{SL}^0}{\left(1 - \frac{\delta}{r_{eq}}\right)^2} d\left(\frac{\delta}{r_{eq}}\right) = 4.65\,978\,581 \gamma_{SL}^0 \qquad (6)$$

Figure 2 shows the surface energy correction for non-equilibrium nucleation concerning dimensionless thickness $\frac{\delta}{r_{Eq}}$. This surface energy correction varies as $1 \le \left(1 - \frac{\delta}{r_{eq}}\right)^{-2} \le\approx 20.39$ and $1 \le \frac{\delta}{r_{Eq}}. \le \frac{\pi}{4}$. Figure 3 presents a comparison among the mean surface energy for pure Al $(\gamma_0 = 0.154\,[\text{J} \cdot \text{m}^{-2}])$, considering $\overline{\gamma_{SL}} = 4.659\,786\gamma_{SL}^0 = 0.7269\,[\text{J} \cdot \text{m}^{-2}]$, and the surface tension, which is very close to the values of the surface tension of pure $\sigma_{SL}^{Al} = 0.914\,[\text{J} \cdot \text{m}^{-1}]$, and that for the aluminum-based alloy Al-6wt%Cu-2.5wt%Si calculated by applying Butler's formulation, $\sigma_{SL}^{Alloy} = 1.0376\,[\text{J} \cdot \text{m}^{-1}]$ [17].

Canté et al. [18] and Jácome et al. [19] have always presented the Gibbs–Thomson coefficient in terms of surface tension for upward solidification kinetics, which according to Eq. 8 represents the mean surface energy. A secondary dendrite arm spacing model proposed by Rappaz and Boettinger [20] for equilibrium solidification and lately modified by Ferreira et al. [17] for non-equilibrium conditions, the surface tension was applied instead of surface energy in the Gibbs–Thomson equation proving a good fit against the experimental scatter. There's no adjustment parameter in both models, as only thermophysical properties, Liquidus tip growth, and solidification local time are provided as input. Concerning the calculation of the critical radius, the mean Gibbs–Thomson coefficient $\overline{\Gamma}$ was chosen to represent
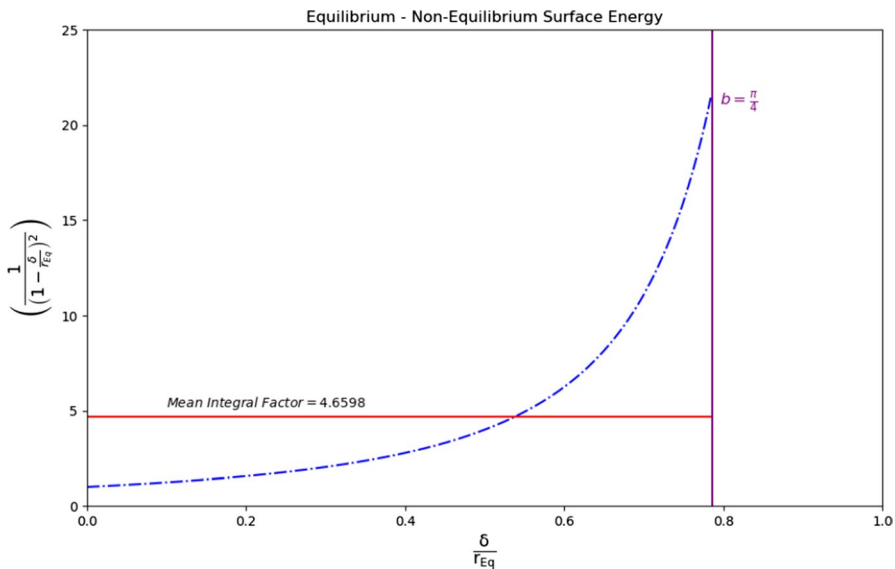

Fig. 2 Surface energy equilibrium/non-equilibrium factor as a function of the dimensionless δ
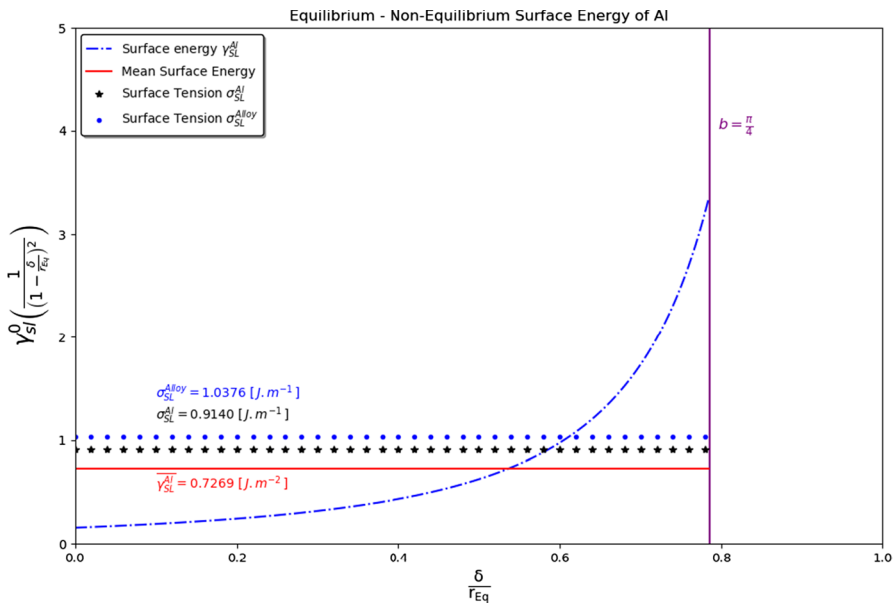
Fig. 3 Surface energy of pure Al equilibrium/non-equilibrium factor as a function of dimensionless delta for Al compared with the surface tension for pure Al and an Alloy

the solidification kinetics between the equilibrium and non-equilibrium conditions, being an essential step in determining the number of modes of the Density of State.

$$\overline{\Gamma} = n_\zeta \frac{\gamma_{sl}^0}{\Delta S_\forall} \zeta = \frac{\sigma_{sl}}{\gamma_{sl}^0} \frac{\gamma_{sl}^0}{\Delta S_\forall} \zeta = \frac{\sigma_{sl}}{\Delta S_\forall} \zeta \cong \frac{4.65\,978\,581 \gamma_{SL}^0}{\Delta S_\forall} \tag{7}$$

where n_ζ is the ratio between surface tension and surface energy, ζ is a spatial parameter assumed as 1 [m]. That's why our definition of Gibbs–Thomson uses surface tension instead of surface energy [13].

2.2 Second Derivation

The relation between the surface stress and surface tension [21–24] is given by,

$$f_{ij} = \delta_{ij}\sigma + \partial\sigma\partial e_{ij} \tag{8}$$

where δ_{ij} is the Kronecker delta, e_{ij} is the elastic component of the strain [24]. In the case of isotropic surface stress,

$$f = \sigma + A\frac{d\sigma}{dA} \tag{9}$$

where A is the surface area.

According to Müller *et al.* [25], surface energy and surface stress are equal for incompressible liquids and are usually merged under a single term of surface tension. The superficial energy dependency on the strain, for no change of heat and no change in the number of surface particles,

$$U^{surf} = \gamma(\varepsilon)A(\varepsilon) = \left(\gamma_0 + \varepsilon\frac{\partial\gamma}{\partial\varepsilon}\bigg|_{\varepsilon=0}\right)A(\varepsilon) \tag{10}$$

and,

$$\gamma(\varepsilon) = \gamma_0 + \varepsilon\frac{\partial\gamma}{\partial\varepsilon}\bigg|_{\varepsilon=0} \tag{11}$$

where γ is the surface energy, ε is the strain. While the definition of surface stress s for isotropic surface gives,

$$s = \frac{\left(\gamma(\varepsilon)A(\varepsilon) - \gamma_0 A_0\right)}{\varepsilon A_0} \tag{12}$$

Analyzing the limit case, Eqs. 9 and 12, by considering $\gamma(\varepsilon)A(\varepsilon) \to 0$ and $\frac{d\sigma}{d\varepsilon} \to 0$,

$$\sigma = \frac{\gamma_0}{-\varepsilon} \tag{13}$$

By considering the schematic representation shown in Fig. 1,

$$\int_0^{-\varepsilon} d\varepsilon = \int_{r_{Eq}-r_{Eq}}^{r_{Eq}-\delta} \frac{8\pi r}{4\pi r_{Eq}^2} dr = \left(1 - \frac{\delta}{r_{eq}}\right)^2 \tag{14}$$

and,

$$\sigma = \frac{\gamma_0}{\left(1 - \frac{\delta}{r_{eq}}\right)^2} \tag{15}$$

Rearranging Eq. 15

$$\frac{\sigma}{\gamma_0} = \frac{1}{\left(1 - \frac{\delta}{r_{eq}}\right)^2} \tag{16}$$

which $\frac{\sigma}{\gamma_0}$ is the surface tension/surface energy relation as a function of δ. Calculating the mean integral of Eq. 16,

$$\left(\overline{\frac{\sigma}{\gamma_0}}\right) = \frac{1}{\frac{\pi}{4}}\int_0^{\frac{\pi}{4}} \frac{d\left(\frac{\delta}{r_{Eq}}\right)}{\left(1 - \frac{\delta}{r_{Eq}}\right)^2} = 4.65978581 \tag{17}$$

The surface energy as a function nucleation radius decrease δ can be obtained by substituting Eq. 14, Eq. 3 into Eq. 12, provides,

$$\gamma(\delta) = \frac{\gamma_0}{\left(1 - \frac{\delta}{r_{Eq}}\right)^2} - s \tag{18}$$

where s is the surface stress. Making s = 0 in the Eq. 16 gives

$$\gamma(\delta) = \frac{\gamma_0}{\left(1 - \frac{\delta}{r_{Eq}}\right)^2} \tag{19}$$

The application of Eq. 17 to several elements is presented in Table 1. Concerning the observed discrepancy for Fe, about the surface tension and surface energy and the mean surface energy, Morohoshi *et al.* [26] calculated surface tension of liquid Fe dependence on O_2 activity a_{O_2} ranging from 1.8 N·m^{-1} to 1.0 N·m^{-1} and compared to experimental data. The surface energy must be measured under the same conditions of the surface tension to achieve the same level of property comparison. The value of 1.0 N·m^{-1} divided by 4.65 978 581 provides 0.214 J·m^{-2}, which is close to 0.204 J·m^{-2} found by Jian *et al.* [27]. The predictions of Eq. 17 compared with the data found in Morohoshi *et al.* are presented in Fig. 4. It suggests the surface energy of Fe is higher for lower activity values of activity of O_2, considering a solution for surface energy found in Kaptay [28], which also could explain the abnormal behavior of the molar heat capacity of Fe, as observed by Ferreira [12] from the data set found in Valencia and Quested [30].

Based on the general model of partial interfacial energy of a component, it is calculated as the change in chemical potential of a given component accompanying the transport of the same component from bulk phase to the interfacial region about the molar interfacial area of the same component. In the case of Fe and O,

Table 1 Comparison between surface energy predictions by Eq. 19 and literature

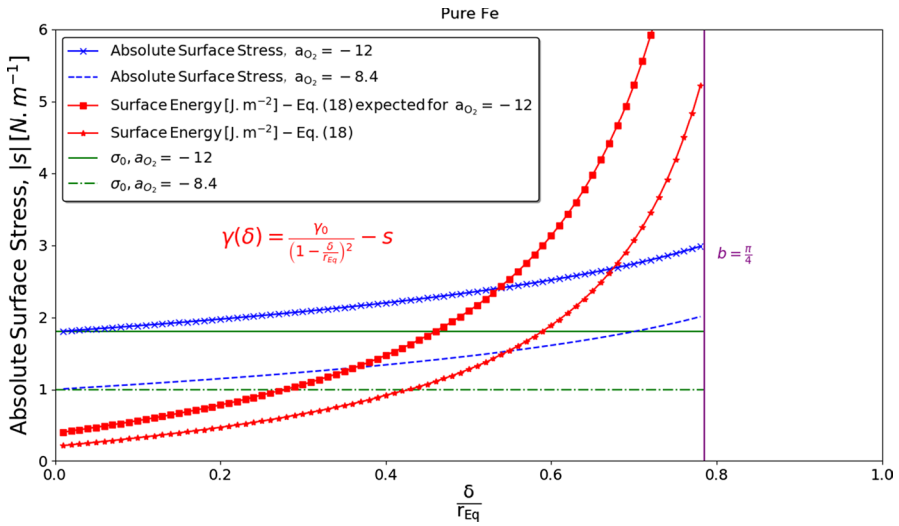| Element	σ at T_m [N·m^{-1}]	Predicted γ^0[J·m^{-2}]	Literature γ[J·m^{-2}]
Al	0.914 [29]	0.196	0.157 [28]
Fe	1.0 [26]*	0.214	0.204 [27]
Cu	1.285 [29]	0.276	0.252 [28]
Ag	0.903 [29]	0.194	0.172 [28]
Au	1.140 [29]	0.245	0.195 [28]
Ni	1.778 [29]	0.382	0.351 [28]
Pd	1.500 [29]	0.322	0.287 [28]
Pt	1.800 [29]	0.386	0.323 [28]

*See Figs. 4 and 5

Fig. 4 Calculation of Fe's absolute surface stress and surface energy as a function of the dimensionless nucleation radius

$$\gamma_{Fe} = \gamma_{Fe}^0 + \frac{RT}{\omega_{Fe}} \ln\left[\frac{1 - x_{O,S/L}}{\sqrt{(1 - x_{O,S})((1 - x_{O,L}))}}\right] + \frac{2\Delta G_{Fe,S/L}^E - \Delta G_{Fe,S}^E - \Delta G_{Fe,L}^E}{2\omega_{Fe}}$$
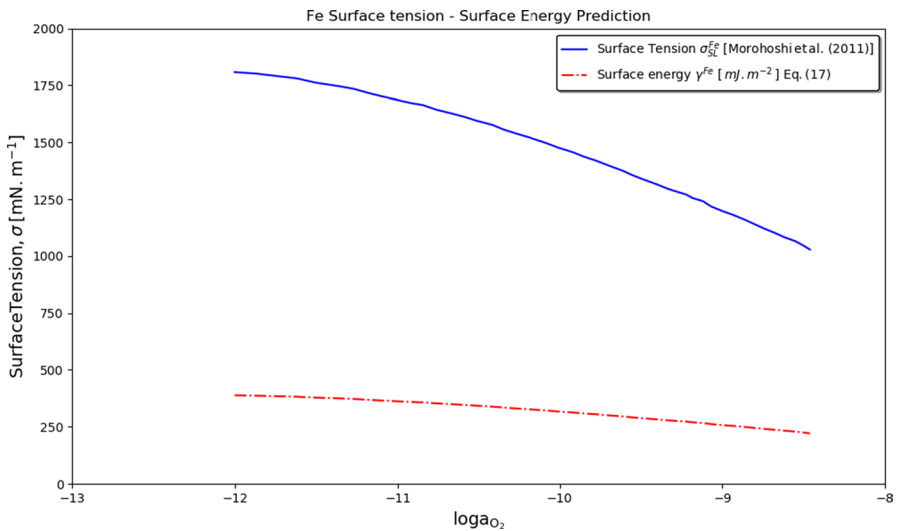
$$(20)$$

Fig. 5 Surface energy prediction by Eq. 17 as a function of the activity of O_2 dependence

Figure 5 presents the absolute surface stress of Fe Eq. 1 and the surface energy Eq. 18, considering the limit values found in Morohoshi *et al.* [26] as a function of the nucleation radius. As can be seen, mean surface tension crosses the surface energy close to its mean value.

The density of state $D\left(\omega_{Comp}\right)$ for a grain of a compound of volume V, with a certain critical nucleation radius, is given by,

$$D_{Comp}\left(\omega_{Comp}\right) = \frac{V\omega_{Comp}^2}{2\pi^2 v^3} \tag{21}$$

where ω_{Comp} is the frequency, v is the speed of sound in the solid. For a total number of atoms N in the volume V and a correspondent density of atoms n provides,

$$N = nV \tag{22}$$

The first Brillouin zone is exchanged by an integral over a sphere of radius k_D, which contains precisely N wave vectors allowed. As a volume of space k by wave vector, it requires,

$$\frac{(2\pi)^3}{V}N = \frac{4\pi k_D^3}{3} \tag{23}$$

Then, the density of atoms n can be obtained as

$$n = \frac{k_D^3}{6\pi^2} = \frac{1}{6\pi^2}\left(\frac{k_B\Theta_{D,Comp}}{\hbar v}\right)^3 \tag{24}$$

The compound fundamental frequencies are expressed as

$$\omega_{D,Comp} = \frac{k_B \cdot \Theta_{D,Comp}}{\hbar} \tag{25}$$

where $\Theta_{D,Comp}$ is the compound Debye's temperature, k_B and $\hbar$ are the constant of Boltzmann and Planck, respectively.

The undercooling for a critical nucleus of volume V can be written for solid–liquid non-equilibrium nucleation as a function of $\delta = r_{Eq} - r$, where $r < r_{Eq}$, written in terms of Eq. 18,

$$\Gamma^{Comp} = \frac{\gamma(\delta)}{\Delta S_\forall^{Comp}} = \frac{\gamma_0 - s\left(1 - \frac{\delta}{r_{Eq}}\right)^2 \Delta S_\forall^{Comp}}{\Delta S_\forall^{Comp}\left(1 - \frac{\delta}{r_{Eq}}\right)^2} \tag{26}$$

and,

$$\Delta T\left(r_C\right) = \frac{2\Gamma^{Comp}}{r_C} \tag{27}$$

Gibbs–Thomson equation, Eq. 26, can be written to express the mean nucleation kinetic through the application of Eq. 17.

The element i electronic contribution c_{ve} is written in terms of the phonon energy c_v^{Vib} as,

$$\frac{c_{ve,i}}{c_v^{Vib}} = \frac{5}{24\pi^3} Z_i \frac{\Theta_{D,i}^3}{T^2 T_{m,i}^{bulk}} \tag{28}$$

where Z_i is the valence of element i, $T_{m,i}^{bulk}$ is the melting temperature of element i [K] and T is the absolute temperature [K].

The rotational energy for each element i, can be given as [11–13],

$$E_{Rot,i} = \frac{5}{4}\hbar^2 \frac{J_i(J_i + 1)}{\overline{M}_i \cdot r_i^2} [J] \tag{29}$$

where J_i is the rotational level corresponding to integer $J = 0, 1, 2, 3, \ldots$, r_i and $\overline{M}_i$ are the atomic radius and the molar mass of element i, respectively. The due to rotation is given by,

$$c_v^{Rot} = \frac{5}{4} \frac{R \cdot \hbar^3 \cdot}{k_B^2 \omega_{D,Comp}(T + \Theta_{D,Comp})^2} \sum_{i=1}^{n} \frac{x_i \cdot J_i(J_i + 1)}{\overline{M}_i \cdot r_i^2} [J \cdot mol^{-1} \cdot K^{-1}] \tag{30}$$

where R is the universal gas constant $[J \cdot mol^{-1} \cdot K^{-1}]$, $\omega_{D,Comp}$ is the maximum admissible frequency known as Debye's frequency.

The obtained final equation molar heat capacity of a compound, which contemplates all contributions is given by,

Table 2 Thermophysical properties of elements

Properties	Unit	Value
Uranium dioxide solid phase density at the melting point—$\rho_{S,UO2}$	$kg \cdot m^{-3}$	9578
Uranium dioxide latent heat—ΔH_{UO2} [ORNL/TM-2000/351] [2]	$J \cdot m^{-3}$	259 300
Uranium atomic radius—r_U	pm	190
Valence of Uranium—Z_U	–	+4
Uranium dioxide Debye's temperature—$\Theta_{D,U02}$ [36]	K	900.0
Planck constant -h	$J \cdot s$	6.626×10^{-34}
Boltzmann constant-k_B	$J \cdot K^{-1}$	$1.380\,658 \times 10^{-23}$
Gas constant -R	$J \cdot mol^{-1} \cdot K^{-1}$	8.314 51

$$c_v = \left(1.0 + D_{Comp}(\omega_{Comp})\right)9N_a k_B \left(\frac{T}{\Theta_{D,Comp}}\right)^3 \int_0^{\frac{T}{\Theta_{D,Comp}}} \frac{x^4 e^x}{(e^x - 1)^2} dx \left(1 + c_{ve}\right)$$

$$+ (n + 1/2)\left[9.0 c_v^{Rot} + \left(1 - \sqrt{\frac{E_i \rho_{Dia}}{E_{Dia}\rho_i}}\right)\frac{RT^3}{\Theta_{D,Alloy}T_L^2}\right]$$

$$(31)$$

3 Results and Discussion

The thermophysical properties used for the calculation of the molar heat capacity are provided in Table 2.

Before assessing the model theoretical prediction of stoichiometric UO_2 molar specific heat capacity some critical considerations must be posed beforehand. A $\lambda-$ transition in solid UO_2 at 2670 K was suggested by Bredig [31, 32], and it is found to take place at the temperature range given by 2670 ± 30 K in stoichiometric UO_2 [33]. They also noticed that The authors explained the high creep rate in terms of the high concentration of oxygen vacancy. Leibowitz *et al.* observed plasticity above 2500 K [34]. Ronchi *et al.*, based on the experimental data explained all the physical contributions to the molar heat capacity. From room temperature to 1000 K the molar heat capacity is governed by harmonic lattice vibration. From 1000 K to 1500 K, the molar heat capacity increases due to non-harmonic lattice vibrations. The highlight of their conclusions in the temperature range from 1500 K to 2670 K is that the increase in the molar heat capacity is provided by the formation
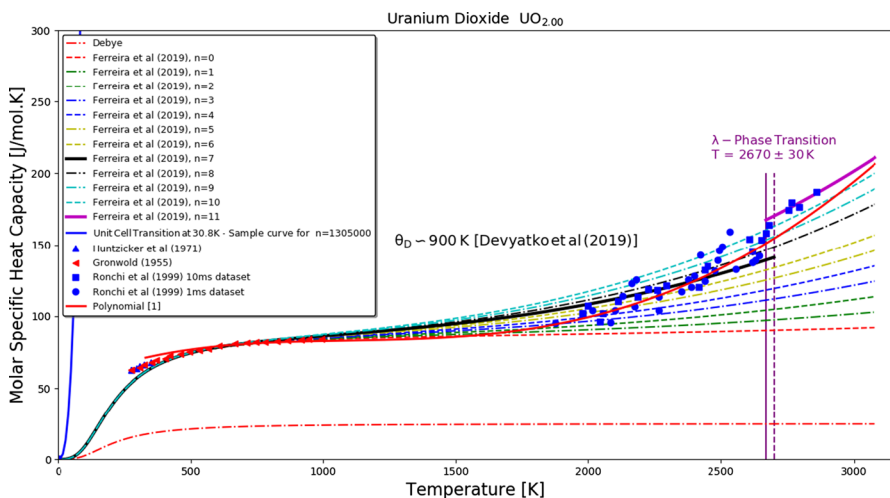

Fig. 6 Comparison of the molar heat capacity of stoichiometric UO_2 and the experimental scatter for low temperature [3, 4] and high temperatures [5]
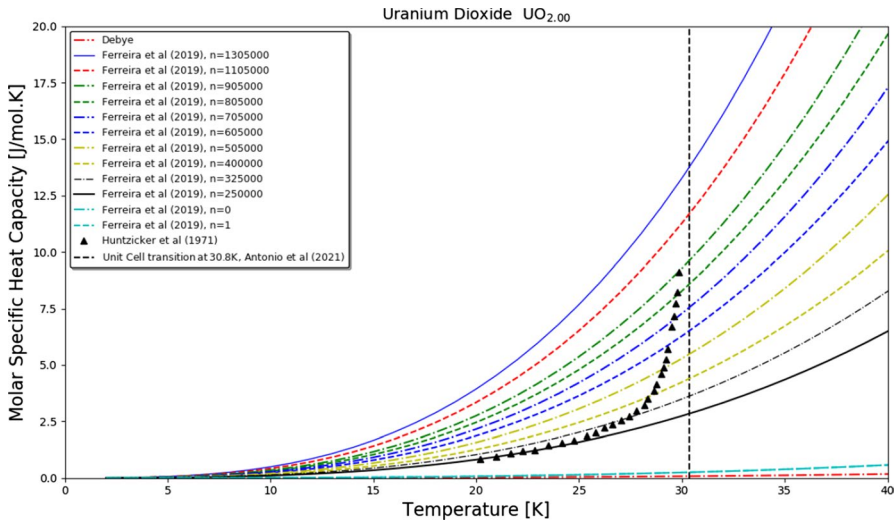
Fig. 7 Low-temperature anti-ferromagnetic high-temperature paramagnetic transition of UO$_2$

of electronic defects and the lattice (Frenkel defects). On the other hand, the increase in the electrical conductivity indicates the contribution from the electronic defects and that electron–hole interactions are minor due to Frenkel defects. Above λ-*phase* transition temperature to the melting point, the Schottky defects become important [35].

Figure 6 represents the molar specific heat capacity of stoichiometric UO$_{2.00}$ predictions Ferreira *et al.* model [11] from 0 K to 2980 K, considering the Debye temperature found in Devyatko *et al.* $\Theta_{D,UO2} \approx 900\,K$ [36]. The λ-*phase* transformation heat predicted by the model is $\Delta H_{\lambda,U02} \approx 28,1612\ J \cdot mol^{-1} \cdot K^{-1}$. Both experimental sets of Ronchi *et al.* [4] are equally distributed around the predicted curve for $n = 7$, due to the thermally induced Frenkel oxygen lattice disorder. From 2670 ± 30 K to 3000 K, where Schottky defects become are more pronounced, making $n = 11$, the model agrees well with the experimental data. This behavior agrees well with a quasi-linear nature of the curve section as described by Ronchi *et al.* [4]. A polynomial curve found in [1] seems to fit the data recognizing the lattice disorder, but it fully neglects the $\lambda-$ transition at 2670 ± 30 K. No simulation was driven considering a non-stoichiometric UO$_{2+x}$. A sample curve for unit cell transition at 30.8 K [8] is provided for $n = 1\ 305\ 000$, further detailed in the next figure. Figure 7 shows a comparison between Ferreira *et al.* [11] model and the experimental data found in Huntzicker and Westrum [3]. High values of *n* corresponding due to the lattice transition kinetic are expected until the limit for molar heat capacity greater than 10 J·mol^{-1}·K^{-1} when it reaches the transformation curve at 30.365 K [3]. Between the limits of the integer range of *n*, for the experimental data of Huntzicker *et*
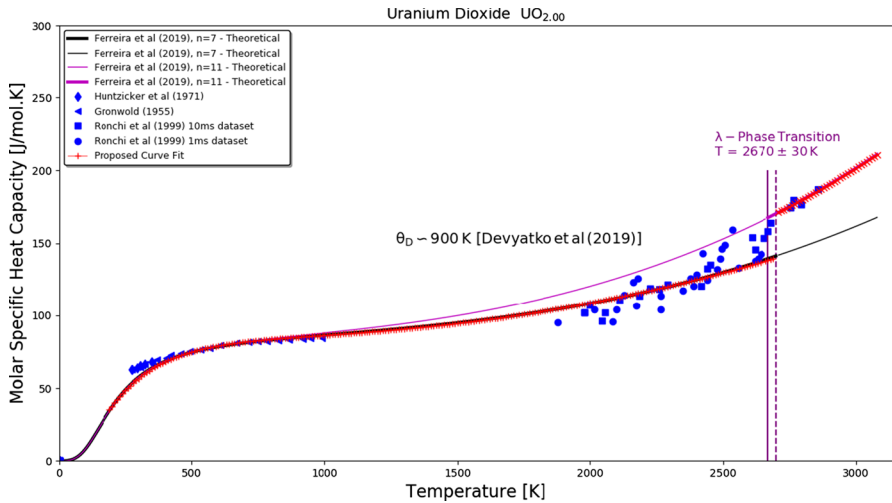
Fig. 8 Comparison of the molar heat capacity experimental, theoretical calculations and the proposed curve fit

al., from 250 000 to 905 000, there are integer numbers inside it which make the model agree precisely.

By considering the theoretical predictions for $n = 7$ and $n = 11$ a curve fit is proposed for the molar specific heat capacity of uranium dioxide in terms of polynomial curve found in [1] and the approximate linear behavior after $\lambda-$ transition as found in Ronchi *et al.* [4].

For $R^2 = 0.9997$ and $30\ K \leq T \leq 2670 \pm 30K$

$$c_v = 92.89\,588\,792 - 19.16\,459\,797\tau + 13.55\,200\,344\tau^2 - 138.3\,100\,784\exp(-4.90\,237\,897\tau) \tag{31a}$$

and, for $R^2 = 0.9999$ and $2670 \pm 30K < T \leq 3138.15K$

$$c_v = 188.37\,506\,432 - 106.35\,673\,004\tau + 36.91\,714\,405\tau^2 \tag{31b}$$

where

$$\tau = \frac{T}{1000} \tag{31c}$$

Figure 8 presents the proposed curve fit for uranium dioxide. As the R-square are very high for the two branches of the curve, it agrees well with the theoretical calculations.

4 Conclusion

The theoretical calculations of the molar specific capacity for stoichiometric uranium dioxide succeed in predicting the temperature ranges' experimental data. The polynomial curve fitted the experimental scatter, where Frenkel oxygen lattice disorder is pronounced. On the other hand, it neglected the λ transition at 2670 ± 30 K completely. Furthermore, the experimental points are equally distributed about the theoretical curve for $n = 7$. In the case of the anti-ferromagnetic to paramagnetic transition, very large values of n must be given. With this point of view, there are a set of large integer numbers in the corresponding interval that simulates the change of specific heat capacity due to this transition. Finally, a quasi-linear behavior was theoretically predicted for temperatures above the λ transition according to what is found in the literature.

References

1. Thermophysical properties database of materials for light water reactor and heavy waters reactors (Iaea-tecdoc). International Atomic Energy Agency, Vienna (2006)
2. S.G. Popov, J.J. Carbajo, V.K. Ivanov, G.L. Yoder. Thermophysical Properties of MOX and UO_2 Fuels Including the Effects of Irradiation. Oak Ridge National Laboratory. US Department of Energy (1996) ORNL/TM-2000/351.
3. J.J. Huntzicker, E.F. Westrum Jr., The magnetic transition, heat capacity and thermodynamic properties of uranium dioxide from 5 to 350 K. J. Chem. Thermodyn. **3**, 61–76 (1971)
4. F. Grønvold, N.J. Kveseth, J. Tichý, Thermodynamics of the UO_{2+x} phase I. Heat capacities of $UO_{2.017}$ and $UO_{2.254}$ from 300 to 1000 K and electronic contributions. J. Chem. Thermodyn. **5**, 665–679 (1970)
5. C. Ronchi, M. Sheindlin, M. Musella, Thermal conductivity of uranium dioxide up to 2900 K from simultaneous measurement of the heat capacity and thermal diffusivity. J. Appl. Phys. **85**, 776–789 (1999)
6. J.K. Fink, M.C. Petri. Thermophysical properties of uranium dioxide. Argonne National Laboratory Report ANL/RE-97/2 (1997)
7. W.M. Jones, J. Gordon, E.A. Long. The heat capacity of uranium, uranium trioxide, and uranium dioxide from 15K to 300K. J. Chem. Phys. **20**, 695–699 (1952)
8. D.J. Antonio, J.T. Weiss, K.S. Shanks, J.P.C. Ruff, M. Jaime, A. Saul, T. Swinburn, M. Solomon, K. Shrestha, B. Lavina, D. Koury, S.M. Gruner, D.A. Anderson, C.R. Stanek, T. Durakiewicz, J.L. Smith, Z. Islam, K. Gofryk, Piezomagnetic switching and complex phase equilibria in uranium dioxide. Commun. Mater. **2**, 17 (2021)
9. M. Jaime, A. Saul, M. Salamon, V.S. Zapf, N. Narrison, T. Durakiewicz, J.C. Lashley, D.A. Anderson, C.R. Stanek, J.L. Smith, K. Gofryk, Piezomagnetism and magnetoelastic memory in uranium dioxide. Nat. Commun. **8**, 99 (2017)
10. K. Gofryk, S. Du, C.R. Stanek, J.C. Lashley, X.-Y. Liu, R.K. Schulze, J.L. Smith, D.J. Safarik, D.D. Byler, K.J. McClellan, B.P. Uberuaga, B.L. Scott, D.A. Andersson, Anisotropic thermal conductivity in uranium dioxide. Nat. Commun. **5**, 4551 (2014)
11. I.L. Ferreira, J.A. de Castro, A. Garcia, Determination of heat capacity of pure metals, compounds and alloys by analytical and numerical methods. Thermochim. Acta **682**, 178418 (2019)

12. I.L. Ferreira, On the heat capacity of pure elements and phases. Mater. Res. **24**, e20200529 (2021)
13. I.L. Ferreira, J.A. Castro, A. Garcia, *On the Determination of Molar Heat Capacity of Transition Elements: From the Absolute to the Melting Point in Book: Recent Advances on Numerical Simulation* (INTECHOPEN, London, 2021). https://doi.org/10.5772/intechopen.96880
14. M.E. Gurtin, A.I. Murdoch, Surface stress in solids. Int. J. Solids Struct. **14**, 431–440 (1978)
15. E.H. Kim, B.J. Lee, Size dependency of melting point of crystalline nano particles and nano wires: a thermodynamic modeling. Met. Mater. Int. **15**, 531–537 (2009)
16. N. Wu, X. Lu, R. An, X. Ji, Thermodynamic analysis and modification of Gibbs-Thomson equation for melting point depression of metal nanoparticles. Chin. J. Chem. Eng. **31**, 198–205 (2021)
17. I.L. Ferreira, A.L.S. Moreira, J. Aviz, T.A. Costa, O.F.L. Rocha, A.S. Barros, A. Garcia, On an expression for the growth of secondary dendrite arm spacing during non-equilibrium solidification of multicomponent alloys: validation against ternary aluminum-based alloys. J. Manuf. Process. **35**, 634–650 (2018)
18. M.V. Cante, J.E. Spinelli, N. Cheung, I.L. Ferreira, A. Garcia, Microstructural development in Al-Ni alloys directionally solidified under unsteady-state conditions. Metall. Mater. Trans. A Phys. Metall. Mater. Sci. **39A**, 1712–1726 (2008)
19. P.D. Jácome, D.J. Moutinho, L.G. Gomes, A. Garcia, A.F. Ferreira, I.L. Ferreira, The application of computational thermodynamics for the determination of surface tension and Gibbs-Thomson coefficient of aluminum ternary alloys. Mater. Sci. Forum **730–732**, 871–876 (2012)
20. M. Rappaz, W.J. Boettinger, On dendritic solidification of multicomponent alloys with unequal liquid diffusion coefficients. Acta Mater. **47**, 3205–3219 (1999)
21. R. Shuttleworth, The surface tension in solids. Proc. Phys. Soc. **63A**, 444–457 (1950)
22. C. Herring, in *The structure and Properties of Solid Surfaces*. eds. R. Gomer, C.S. Smith (University of Chicago Press, Chicago, 1952), p. 5
23. W.W. Mullins, *Metal Surfaces: Structure* (Energetics and Kinetics. American Society for Metals, Ohio, 1962), p. 17
24. J.S. Vermaak, C.W. Mays, D. Juhlmann-Wilsdorf, On the surface stress and surface tensor: I. Theoretical considerations. Surf. Sci. **12**, 128–133 (1968)
25. P. Müller, A. Saul, F. Leroy, Simple views on surface stress and surface energy concepts. Nanosci. Nanotechnol. **5**, 013002 (2014)
26. K. Morohoshi, M. Uchikoshi, M. Isshki, H. Fukuyama, Surface tension of liquid iron as functions of oxygen activity and temperature. ISIJ Int. **51**, 1580–1586 (2011)
27. Z. Jian, K. Kuribayashi, W. Jie, Solid-liquid interface energy of metals at melting point and undercooled state. Mater. Trans. **43**, 721–726 (2002)
28. G. Kaptay, On the solid/liquid interfacial energies of metals and alloys. J. Mater. Sci. **53**, 3767–3784 (2018)
29. C.J. Smithells, *General Physical Properties, Metals Reference Book*, 7th edn. (E.A, 1998)
30. J.J. Valencia, P. Quested, Thermophysical Properties. Casting. ASM Handb. ASM Int. **15**, 468–481 (2008)
31. M.A. Bredig, in *L'etude des Transformations Crystalline a Hautes Temperatures*, Proceedings of a Conference held in Odeillo, France, 1971 (CNRS, Paris, 1972), p. 183
32. M.T. Hutchings, High-temperature studies of UO_2 and ThO_2 using neutron scattering techniques. J. Chem. Soc. Faraday Trans. II **83**, 1083–1103 (1987)
33. J.P. Hiernauts, G.J. Hyland, C. Ronchi, Premelting transition in uranium dioxide, int. J. Thermophys. **14**, 259–283 (1993)
34. L. Leibowitz, J.K. Fink, O.D. Slagle, Phase transitions, creep, and fission gas behavior in actinide oxides. J. Nucl. Mater. **116**, 324–325 (1983)
35. C. Ronchi, G.J. Hyland, Analysis of recent measurements of the heat capacity of uranium dioxide. J. Alloys Compd. **213**, 159–168 (1994)
36. Y.N. Devyatko, V.V. Novikov, O.V. Khomyakov, D.A. Chulkin, A model of uranium dioxide thermal conductivity. Inorg. Mater. Appl. Res. **7**, 70–81 (2017)